Pergamon

J. Mech. Phys. Solids, Vol. 44, No. 1, pp. 23–48, 1996

0022-5096/96 $15.00+0.00

0022-5096(95)00068-2

FRACTURE MECHANICS FOR THE DESIGN OF CERAMIC MULTILAYER ACTUATORS

T. H. HAO

Division of Basic Sciences, China Textile University, Shanghai, China

X. GONG and Z. SUO

Mechanical and Environmental Engineering Department, Materials Department, University of California, Santa Barbara, CA 93106, U.S.A.

(*Received* 5 *May* 1995; *in revised form* 4 *August* 1995)

ABSTRACT

In a multilayer actuator, each internal electrode terminates an edge inside the active ceramic. Around the edge, the nonuniform electric field generates an incompatible strain field, which, in its turn, generates stresses and may cause the ceramic to crack. The industry has been exploring alternative electrode configurations to alleviate the stress concentration. The effort has been empirical and benefited little from numerical simulations. An inherent difficulty is that the actuator ceramics have nonlinear electro-mechanical interactions, of which no unified mathematical description is now available. In this paper, we develop a crack nucleation model that includes essential features of this nonlinearity. The model applies to both paraelectrics and ferroelectrics. Attention is focused on situations where the small-scale saturation conditions prevail. That is, the driving voltage is low enough so that the bulk of the ceramics is linearly dielectric, except for a cylinder of a small radius around the electrode edge. Inside the cylinder, large strains result from electrostriction or polar rotation. We identify a parameter group that determines the cracking condition; details in the material description only affect a dimensionless coefficient. Everything else being fixed, a critical layer thickness exists, below which a multilayer actuator will not crack around its internal electrode edges. Merits and limitations of the small-scale saturation model are discussed. We analyze this model analytically for a paraelectric with perfect polarization saturation, and estimate the value of the dimensionless coefficient in the model.

1. INTRODUCTION

Subject a dielectric oxide to an electric field, cations and anions displace somewhat in the opposite directions, giving rise to both a polarization and a distortion. The latter effect forms the basis of a family of solid state devices, the actuators. They deliver motions upon receiving electrical signals. An electric field about 1 MV/m induces strains of magnitude 10^{-4}–10^{-2} in many perovskite-type oxides. For a moderate voltage to deliver an appreciable motion, an actuator is made of hundreds of ceramic layers alternating with thin film metallic electrodes. Figure 1(a) sketches a basic design. Each ceramic layer, thickness H, is under the same voltage, V, so that the electric field is $E_{\text{appl}} = V/H$ everywhere in the ceramic except for the edge. A 100 μm thick layer, for example, needs 100 V driving voltage to attain 1 MV/m electric field. Uchino (1993) surveyed the applications of the devices in technologies.

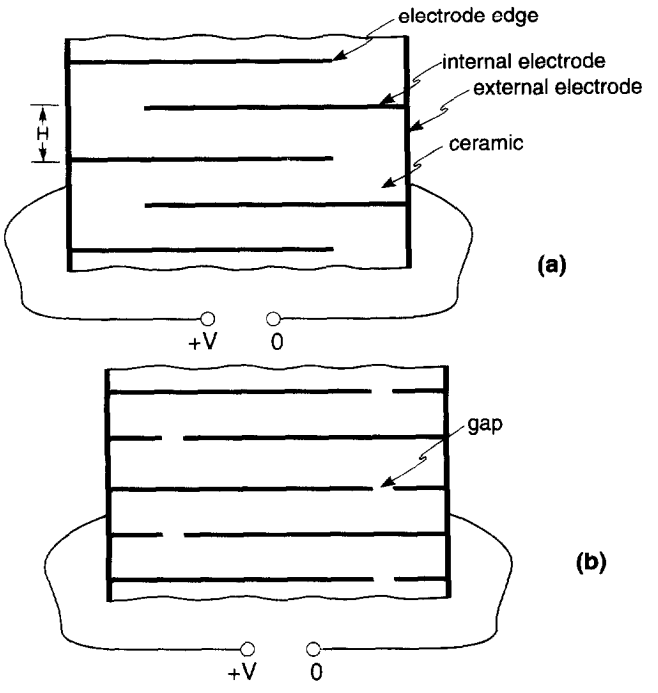

Fig. 1. Two basic designs of ceramic multilayer actuators. (a) Each internal electrode terminates an edge inside the ceramic. (b) A gap lies on each electrode.

Inherent in the design is that each electrode terminates an edge inside the ceramic. The driving voltage induces a stress field around the electrode edge. Each actuator, operating for millions of cycles, has hundreds of such stress concentration sites. They have raised serious reliability concerns. Experiments have demonstrated that an actuator can crack around its internal electrode edges when each layer is thick and the ceramic has a large electric-field-induced strain (Furuta and Uchino, 1993; Aburatani *et al.*, 1994; Schneider *et al.*, 1994). The latter is particularly disturbing. Can we use ceramics capable of larger strains? The industry has been exploring alternative designs to alleviate the stress concentration, one of which is sketched in Fig. 1(b). Yoshikawa and Shrout (1993) surveyed the cost–performance–reliability relationships among the proposed designs.

Analyzing the stress field around electrode edges has been difficult. Even when the actuator is under a moderate nominal electric field, E_{appl}, the field intensifies around the electrode edges. A unifying description is still unavailable of the nonlinear interactions under multiaxial and cyclic loads, although most outstanding aspects have been known for many years. Winzer *et al.* (1989) analyzed the stress concentration using finite elements for a linear dielectric with quadratic electrostriction. From the work of Smith and Warren (1966) and McMeeking (1987), it is known that this material model leads to a $1/r$ singular stress field around an electrode edge.

Suo (1993) introduced a model for an initially unpoled ferroelectric, where the intense electric field rotates polar axes near the electrode edge, resulting in an incom-

patible strain field. Without relying on any detailed form of the constitutive law, this model gives the cracking condition with a parameter group. Yang and Suo (1994) extended this model to an ideal electrostrictive material, and estimated the magnitude of the stress intensity factors on the flaws around the electrode edges. Gong (1994) formulated a finite element model on the basis of more realistic descriptions of electrostrictive ceramics. Gong and Suo (1995) will report further details on finite element implementation and results.

The plan of this paper is as follows. Section 2 gives a synopsis of the nonlinear interactions of the actuator ceramics. We will qualitatively describe both paraelectrics and ferroelectrics, and review a constitutive law for the former. Section 3 casts the model of Suo (1993) and Yang and Suo (1994) into a form convenient for actuator design. Section 4 presents an analytic solution of the model with a more realistic material description.

2. ELECTRO-MECHANICAL INTERACTIONS OF ACTUATOR CERAMICS

Electro-mechanical fields obey the partial differential equations listed in Appendix A. To determine the fields, e.g. around an electrode edge, one must also prescribe a relation of strain and electric displacement to the loading history of stress and electric field. Exactly what to prescribe is still an unsolved problem for the actuator ceramics in general. In this section, we give a synopsis of the nonlinear interactions. Most phenomena originate from a few simple facts of the crystal structures. It is, therefore, worthwhile to recall them before we review the behaviors of the ceramics.

The perovskite family

Perovskite ($CaTiO_3$) is a mineral of little use, but has a crystal structure similar to many prominent oxides. Barium titanate ($BaTiO_3$) is the first distinguished member in this family (see Jona and Shirane, 1962). It undergoes a phase transition at a temperature about 130 C. Figure 2 illustrates the crystal structures of the two phases, the paraelectric and the ferroelectric. Above 130 C, the crystal is cubic, and the ions lie symmetrically in the unit cell: the positive and the negative charge centers both coincide with the cube center. Between 0 and 130 C, the crystal is tetragonal, and the ions lie asymmetrically in the unit cell; the positive and the negative charge centers separate from each other. At the room temperature, for example, the tetragonal phase has lattice constants $a = 3.992$ Å and $c = 4.032$ Å, and a polarization $P_s = 0.26\ \mathrm{C/m^2}$.

The cubic phase barium titanate is a nonpolar crystal. Under an electric field, the crystal polarizes (permittivity) and deforms (electrostriction). Under the same electric field, ions in barium titanate displace several orders of magnitude more than ions in a common dielectric such as silica, giving barium titanate its large permittivity coefficient and electrostrictive strains. Under a stress, the crystal deforms elastically but does not polarize.

The tetragonal phase barium titanate is a polar crystal. It differs, however, in an important way, from common polar molecules and crystals (e.g. water and gallium

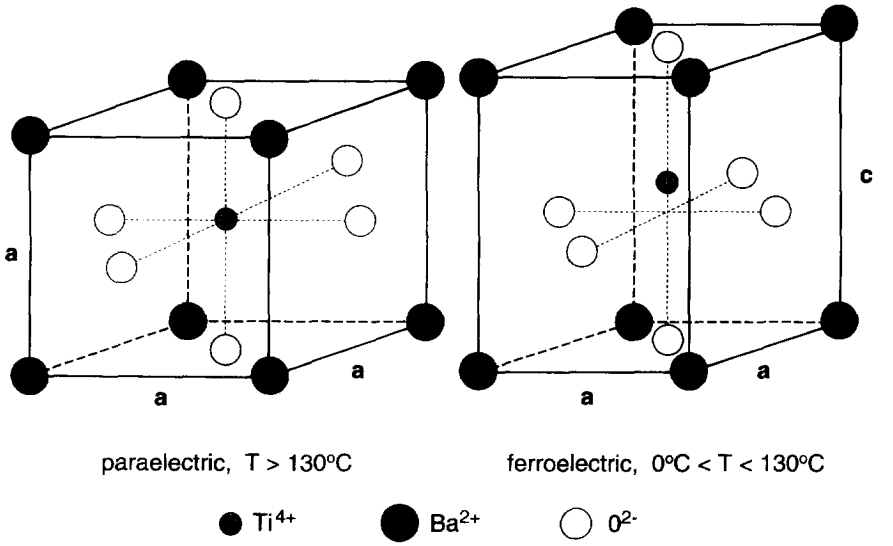

Fig. 2. The crystal structures of barium titanate ($BaTiO_3$). The high temperature phase is nonpolar. The low temperature phase is polar and the Ti^{4+} is off the cell center.

arsenide). Upon cooling through the transition temperature, a tetragonal unit cell takes any one of the six variants of the polar direction. An electric field or a stress can switch the crystal from one variant to another. The process is analogous to mechanical twinning. Figure 3 illustrates several possibilities. For example, an electric field, applied in a direction different from the existing polar direction, shifts the ions such that the new polar direction aligns, as closely as possible, with the electric field. An electric field can rotate the polar direction by either 180° or 90°, but a stress can only rotate it by 90°. They exemplify, respectively, the ferroelectric and the ferroelastic phenomena. A 180° polar rotation does not result in any strain. A 90° polar rotation results in an enormous strain, $(c-a)/a = 0.01$. Before and after polar rotation, an electric field also causes the ions to move slightly around their equilibrium positions, resulting in the piezoelectric strains. They vary linearly with the electric field and are much smaller than the strain associated with the 90° switching.

Many perovskite-type oxides and their solid solutions have similar properties. They may take different crystalline symmetries, and may change phases as the temperature or the composition changes. The materials are used in polycrystalline, i.e. ceramic forms. At the room temperature, they can be in paraelectric, ferroelectric, or other phases (e.g. Pan *et al.*, 1989). A lead magnesium niobate $PbMg_{1/3}Nb_{2/3}O_3$ (PMN), doped with lead titanate, is a relaxor-ferroelectric, and has macroscopic responses similar to those of a paraelectric (Jang *et al.*, 1980; Winzer *et al.*, 1989). The most widely used ferroelectrics are $PbTiO_3$–$PbZrO_3$ solid solutions, commonly known as PZT (Jaffe *et al.*, 1971). Small amounts of other elements added to the basic composition can ease fabrication or tailor properties. For example, a lanthanum-doped PZT, known as PLZT, has an unusual property: it is transparent to light even in ceramic form, and is used as optical sensors (Haertling, 1987).

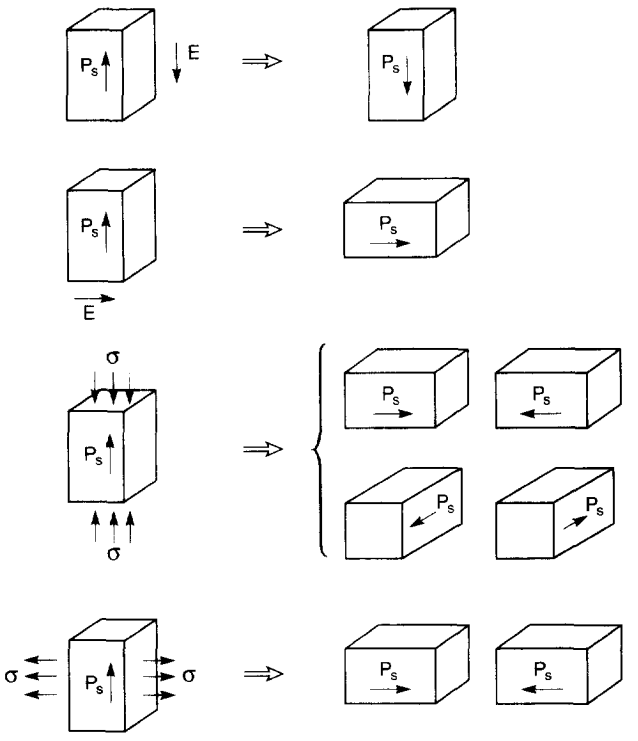

Fig. 3. In the ferroelectric phase, barium titanate has six variants of the polar direction. An electric field or a stress can switch the crystal from one variant to another.

Ceramics in paraelectric phase

For a ceramic in the paraelectric phase or a relaxor-ferroelectric that behaves like a paraelectric, the matter of formulating a constitutive law is greatly simplified because the material is, to a good approximation, isotropic and history-independent. Sketched on the left-hand side in Fig. 4 are paraelectric responses under uniaxial loads. In the absence of the stress, an electric field E induces an electric displacement D. The D–E relation is nonlinear, designated by a function

$$E = f(D). \tag{2.1}$$

At small electric fields, D increases linearly with E, and the slope defines the permittivity, ε, namely,

$$D = \varepsilon E, \quad E \to 0. \tag{2.2}$$

The permittivity is enormous for many perovskite-type oxides ($\varepsilon/\varepsilon_0 = 10^3$–$10^5$). When the electric field exceeds about 1 MV/m, ionic movements become difficult with further increase in the electric field, so that the D–E curve is flat (relative to its initial slope). The phenomenon is called polarization saturation. A comparison with a common dielectric is illuminating. Silica has a small permittivity ($\varepsilon/\varepsilon_0 < 10$), and has essentially a linear D–E relation up to its dielectric breakdown field (> 100 MV/m).

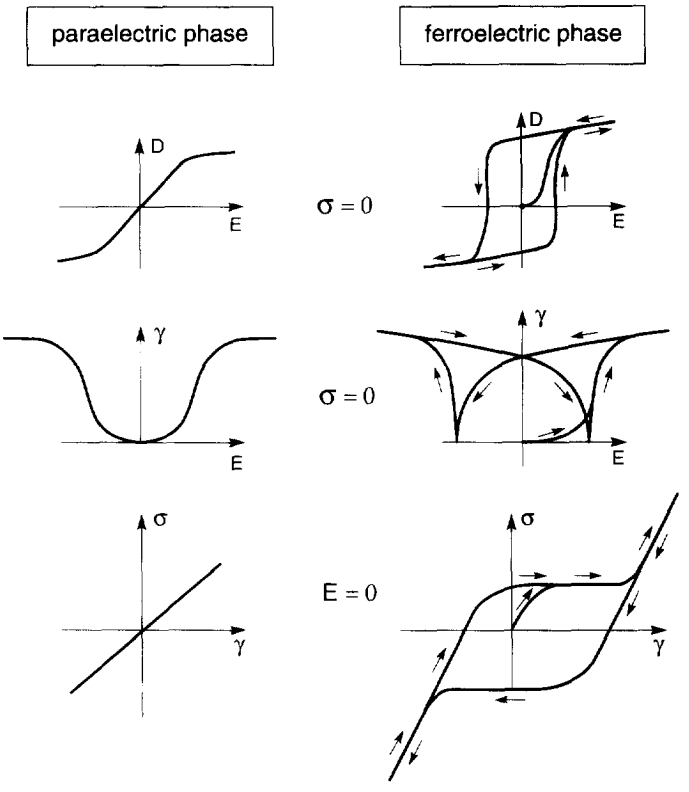

Fig. 4. Nonlinear electro-mechanical interactions of a paraelectric and a ferroelectric. A paraelectric exhibits no hysteresis, and a ferroelectric exhibits hysteresis.

In the absence of stress, the electric field also induces electrostriction : a longitudinal elongation strain γ_L and a transverse contraction strain γ_T. For an isotropic ceramic, two electric fields, of the same magnitude but applied in the opposite directions, cause identical distortion, so that the γ E curve is symmetric. At small electric fields, the strains are proportional to E^2. For example, the longitudinal strain is

$$\gamma_L = ME^2, \quad E \to 0, \tag{2.3}$$

where M is a material constant. At large electric fields, the strains also saturate when the electric displacement saturates, so that (2.3) is incorrect at large electric fields.

Sundar and Newnham (1992) introduced a simplification on the basis of experimental data. To a high accuracy, even at large electric fields, the strains are proportional to the electric displacement squared, $\gamma \propto D^2$. They argued that this correlation is not fortuitous since both the strains and the electric displacement are the manifestations of the same physical process, the ionic movements. We adopt their description. An electric displacement (in the absence of stress) induces the longitudinal and transverse strains

$$\gamma_L = QD^2, \quad \gamma_T = -qQD^2, \tag{2.4}$$

Table 1. *Data of an electrostrictive ceramic used in numerical examples*

$\varepsilon/\varepsilon_0$	Y	ν	Q	q	γ_s	K_{Ic}
7500	114 GPa	0.26	0.021 $m^4 C^{-2}$	0.38	10^{-3}	0.9 $MPa\sqrt{m}$

The vaccum permittivity $\varepsilon_0 = 8.85 \times 10^{-12} F/m$.

where Q is the electrostrictive coefficient, and q a dimensionless number. Note that $M = Q\varepsilon^2$. We assume that the electrostrictive strains obey (2.4) at both small and large electric fields.

In the absence of the electric field, stresses induce strains that obey Hooke's law (e.g. Cao and Evans, 1993). Under a uniaxial stress σ, the longitudinal and the transverse strains are

$$\gamma_L = \sigma/Y, \quad \gamma_T = -\nu\sigma/Y, \tag{2.5}$$

where Y is Young's modules, and ν Poisson's ratio.

The total strains are taken to be the superposition of the effects of elasticity and electrostriction, namely,

$$\gamma_L = \frac{\sigma}{Y} + QD^2, \quad \gamma_T = -\nu\frac{\sigma}{Y} - qQD^2. \tag{2.6}$$

The stress also affects the electric displacement according to

$$E = f(D) - 2Q\sigma D. \tag{2.7}$$

The second term arises from a thermodynamic consideration, and is typically negligible compared to the first term.

Suo (1991) and Hom and Shankar (1994) have extended this constitutive law to multiaxial loading conditions. See Appendix B for a summary. Table 1 lists data to be used in numerical estimates and plots in this paper; they are representative of a relaxor-ferroelectric (Jang *et al.*, 1980; Winzer *et al.*, 1989; White and Friedman, 1994).

Ceramics in ferroelectric phase

Upon cooling from the paraelectric to the ferroelectric phase, a polycrystalline aggregate forms a complicated pattern of domains, each having its own polar direction. No polarization appears at the macroscopic scale. The ceramic can be poled by an electric field. To our knowledge, no general constitutive laws are available for ferroelectrics. The difficulty arises from hysteresis and multiaxial loading. The strain and electric displacement depend not only on the current stress and electric field, but also on the loading history. Data of electric displacements and strains are available under uniaxial electric field (e.g. Jaffe *et al.*, 1971), uniaxial stress (Cao and Evans, 1993), and their combinations (Lynch *et al.*, 1994; Lynch, 1995). We are unaware of any systematic tests under multiaxial loading conditions. Note that, for an initially poled ceramic, a transverse electric field generates larger strains than a longitudinal

electric field, since the former induces larger amount of 90° polar rotation. This effect is expected to be important for cracking phenomena.

The right-hand side of Fig. 4 illustrates responses of an initially unpoled ferroelectric under uniaxial loads. First look at the effects of an electric field in the absence of stress. At a small electric field, the ceramic is linearly dielectric—the electric displacement increases linearly with the electric field. At a large electric field, polar rotation starts progressively via domain wall motion. Energy barriers, such as impurities or space charges, exist to impede the wall motion so that switching only occurs at sufficiently high electric fields. Switching completes with a substantial increase in the electric displacement. Afterwards, the material becomes linearly dielectric again. Upon unloading and reloading, the state (D, E) cycles around a hysteresis loop.

In the absence of stress, the electric field also distorts the ceramic. Figure 4 shows the longitudinal strain as a function of the applied electric field. A small electric field induces electrostrictive strains. At a larger electric field, when the polar rotation starts, the strain increases substantially with a small increase in the electric field. After the switching is completed, the ceramic becomes linearly piezoelectric—the strain increases with the electric field linearly with a shallow slope. Upon unloading and reloading, the state (γ, E) cycles around a butterfly-shaped hysteresis loop. Depending on the material, the lowest strain on the hysteresis loop may lie either above or below the reference strain of the unpoled state. Due to the complex internal interactions, a ferroelectric ceramic cycling under a uniaxial electric field deforms appreciably.

Next consider an initially unpoled ceramic loaded with a uniaxial stress (both tension and compression), but under no external electric field. Figure 4 shows the longitudinal strains at various stresses. At a small stress the material is linearly elastic. Above some stress level, when the polar rotation starts, the strain increases substantially for a small increase in the stress. The ceramic becomes linearly elastic after the switching is completed. Upon unloading and reloading, state (σ, γ) cycles around a hysteresis loop. The stress alone does not pole a ferroelectric.

3. CRACKS EMANATING FROM AN ELECTRODE EDGE

Crack nucleation and its stable growth

Figure 5 illustrates the crack nucleation model proposed by Suo (1993) and Yang and Suo (1994). Under a driving voltage, electrostatics dictate that the field lines approach the electrodes perpendicularly [Fig. 5(a)]. Near the edge the field is intense and nonuniform [Fig. 5(b)], inducing incompatible strains and, thereby, stresses. Cracks nucleate when the stresses extend over a large enough volume and interact with the flaws in the ceramic.

After nucleating near the electrode edge, a crack may extend stably by several processes. If a conducting species migrates on the freshly created crack surface, the crack itself becomes a conducting sheet. The stress will concentrate at the edge of the sheet and extend the crack. If conducting species is unavailable, the stress due to the presence of the electrode edge will diminish as the crack extends away. It has been observed, however, that cracks bifurcate and extend in ferroelectrics under cyclic

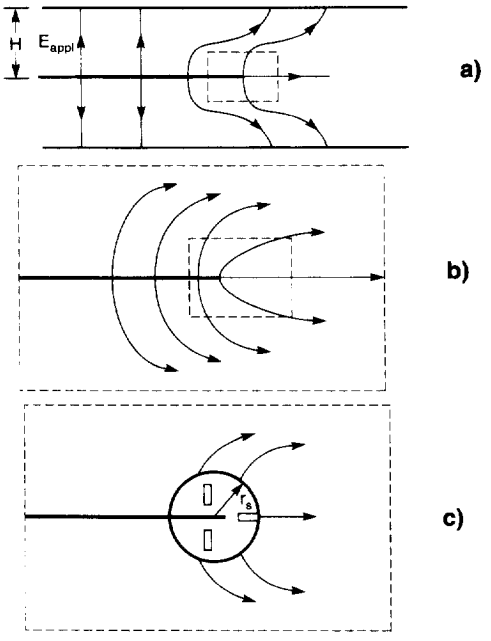

Fig. 5. The small-scale saturation model. (a) The field lines approach the electrodes perpendicularly. (b) The field around the electrode edge. (c) The intense electric field rotates polar directions inside a cylinder around the electrode edge (drawn for an initially unpoled ferroelectric).

electric field (Furuta and Uchino, 1993; Aburatani *et al.*, 1994; Schneider *et al.*, 1994). These cracks appear to be driven by the stress concentration at the crack tip associated with ferroelectric switching. In this connection, we call attention to a less known phenomenon. Cao and Evans (1994) and Lynch *et al.* (1995) demonstrated experimentally that a crack can grow stably in a ferroelectric, in a direction nominally perpendicular to the electric field lines, under cyclic electric field exceeding the coercive field. The two phenomena appear to have a similar physical origin.

The existing understanding does not permit us to conclude whether crack nucleation or its stable growth is more threatening to actuator reliability. In this paper, we focus on crack nucleation around an electrode edge in a paraelectric or an initially unpoled ferroelectric. We will neglect effects secondary to the large strains associated with electrostriction (in the paraelectric) or polar rotation (in the ferroelectric). Following Smith and Warren (1966) and Winzer *et al.* (1989), we will ignore the effect of the stress on the electric displacement. The electrode is taken to be a plane of vanishing thickness.

Small-scale saturation model for crack nucleation

In this subsection we assume that the nominal electric field, $E_{appl.}$ is small so that the major portion of the ceramic is linearly dielectric, except in a small volume around the edge. We will call this the small-scale saturation condition, and the small volume

the saturated cylinder. The merits of the small-scale saturation will become evident later.

If the ceramic were linearly dielectric all the way to the electrode edge, the electric field would be square-root singular [Fig. 5(b)]. For example, the electric field a distance r ahead of the electrode edge would be

$$E = \frac{K_E}{\sqrt{2\pi r}}. \tag{3.1}$$

This field distribution is approximately valid in a hollow cylinder, whose inner radius is larger than the saturated cylinder, and outer radius smaller than the ceramic layer thickness.

The electric intensity factor, K_E, depends on the driving voltage and the device geometry, and is determined from linear dielectric boundary value problems that ignore the nonlinearity around the electrode edge. Linearity and dimensional considerations dictate that K_E scale with the nominal electric field E_{appl} and layer thickness H according to

$$K_E = \Omega E_{appl}\sqrt{H}. \tag{3.2}$$

The dimensionless coefficient Ω depends on the device geometry, i.e. on the ratios of the various lengths in Fig. 1.

Near the electrode edge the intense electric field induces nonlinear interactions [Fig. 5(c)]. Denote E_s as the electric field at which nonlinearity becomes important. For a paraelectric, E_s may be identified as the electric field at which the electric displacement almost saturates. For a ferroelectric, E_s may be identified as the field causing substantial polar rotation. Naturally, this quantity can be identified rigorously once a material model is specified. One can estimate the radius of the saturated cylinder, r_s, by letting $E = E_s$ in (3.1). It scales as $r_s \approx (K_E/E_s)^2/2\pi$. The saturated cylinder enlarges as the driving voltage increases. The exact size, shape and position of the saturated cylinder depend on the details of the material description. They are of secondary importance in this model.

Associated with the large electric field is a strain, γ_s. For a paraelectric, γ_s may be identified as the saturated electrostrictive strain. For a ferroelectric, γ_s may be identified as the strain associated with polar rotation. Around the electrode edge, the electric field is nonuniform and generates an incompatible strain field, which, in its turn, generates a stress field. This stress field can be determined when a material description is prescribed. Its salient features, however, can be inferred readily. The stress field is localized within a region scaled by r_s, and decays sharply away from the cylinder. The magnitude of the stress scales with $Y\gamma_s$, with Y being an elastic modulus. A tensile stress arises in the plane directly ahead of the electrode edge, as expected from the electric field lines and the associated distortions in Fig. 5(c).

The phenomenon is similar to cracking around inclusions caused by thermal expansion mismatch (Lange, 1974; Lu *et al.*, 1991). As pointed out by Lange (1974), a localized stress field interacts with flaws in a way different from a uniform stress field. In a uniform stress field, a flaw, once activated, grows catastrophically. In a localized

stress field, the stress intensity factor, K_I, is small for both small and large flaws, and peaks for a flaw of some intermediate size, so that an activated flaw will arrest.

In our problem, the size of the flaw that acquires the maximum stress intensity factor scales with the radius of the saturated cylinder, r_s. Dimensional considerations dictate that the maximum stress intensity factor should scale as $(K_I)_{max} \propto Y\gamma_s\sqrt{r_s}$. Combining with the formula for r_s, we find that the maximum stress intensity factor is

$$(K_I)_{max} = \Lambda \frac{Y\gamma_s K_E}{E_s} \tag{3.3}$$

for all the flaws around the electrode edge. The dimensionless coefficient Λ depends on the details in the material description.

Denote the toughness of the ceramic by K_{Ic}. Only the intrinsic toughness resists the nucleation of a small crack. The dissipative processes—switching and grain sliding—make no contribution. No flaws, of any size and at any location, can grow if $(K_I)_{max} < K_{Ic}$. Combining with (3.2), we find that an actuator will never crack if

$$\frac{K_{Ic}E_s}{Y\gamma_s\sqrt{HE_{appl}}} > \Lambda\Omega. \tag{3.4}$$

This dimensionless group consists of the material properties, the driving voltage, and the ceramic layer thickness.

The cracking condition (3.4) can be written

$$H_c = \left(\frac{K_{Ic}E_s}{\Lambda\Omega Y\gamma_s E_{appl}}\right)^2. \tag{3.5}$$

Consequently, for a given geometry, material and driving field, a critical layer thickness H_c exists, below which an actuator will not crack around the electrode edges. Now we are better informed to answer the question raised in the Introduction: Can we use ceramics capable of larger strains? The answer is yes, provided each layer can be made thinner. The following examples illustrate the tradeoff.

Numerical examples

We now apply the model to the design in Fig. 1(a). Assuming that the spacing between the internal electrode edge and the ceramic layer end is large enough relative to the layer thickness, Suo (1991) showed that the actuator has the electric intensity factor

$$K_E = E_{appl}\sqrt{2H}. \tag{3.6}$$

Thus, the dimensionless coefficient defined in (3.2) is $\Omega = \sqrt{2}$ for this design.

The radius of the saturated cylinder is estimated by

$$r_s \approx \frac{H}{\pi}\left(\frac{E_{appl}}{E_s}\right)^2. \tag{3.7}$$

The cylinder enlarges as the driving voltage increases. For example, when $E_{appl} = E_s/2$, the cylinder has radius $r_s \approx H/12$. It seems reasonable to expect the small-scale saturation to be a reasonable approximation under this circumstance.

The numerical coefficient defined by (3.3) is estimated to be $\Lambda = 0.19$ from an ideal paraelectric analyzed by Yang and Suo (1994). With a more realistic material description, we obtain $\Lambda = 0.13$ in Section 4 of this paper. The latter value, together with (3.4) and (3.6), shows that an actuator will not crack if

$$\frac{K_{Ic}E_s}{Y\gamma_s\sqrt{H}E_{appl}} > 0.18. \tag{3.8}$$

Using the material data in Table 1, and taking the nominal field to be $E_{appl} = E_s/2$, we find that the critical layer thickness is $H_c = 7.7$ mm. Since in practice the ceramic layers are much thinner than this value, actuators made of the material defined by Table 1 should not crack by this mechanism. However, for a material with a larger saturation strain, $\gamma_s = 5 \times 10^{-3}$, everything else being the same, the critical thickness reduces to $H_c = 308$ μm. These values are consistent with the experimental findings of Furuta and Uchino (1993) and Aburatani *et al.* (1994). While the comparison is encouraging, one must not attach much significance to the numbers at this point, for the model has only been analyzed for an ideal paraelectric.

The merits of the small-scale saturation model

The square-root singular field (3.1) is valid only in the hollow cylinder, $r_s \ll r \ll H$. Consequently, the small-scale switching model is correct only when $r_s \ll H$. The limitation of the idea is obvious, given that the actuators may operate near the saturation strains when the bulk of the ceramic layer is nonlinear. Its merits, however, justify an effort to check just how good this approximation might be. Let us look at what is involved in using this approach as opposed to a complete nonlinear analysis.

The small-scale saturation approach separates the two aspects of an actuator: the geometry and the material. For an electrode geometry, a solution of linear dielectric boundary value problem determines the electric intensity factor, K_E. Various length ratios only affect the dimensionless coefficient Ω defined by (3.2). The results, once obtained from the geometry, are applicable to all materials. A compilation of the electric intensity factors for the key actuator designs appears to be imperative.

The material nonlinearity only affects the dimensionless coefficient Λ defined by (3.3), and is independent of the device geometry. Given the present status of the constitutive laws for the actuator ceramics, it is unlikely this coefficient will be rigorously calculated for every single material from numerical simulations. Rather, a more fruitful approach would be to calibrate this coefficient by combining experiments with calculations on the basis of ideal material descriptions.

As demonstrated in the above numerical examples, once Ω and Λ are determined separately, one can determine, at least broadly, whether a geometry or a material will be viable. Even in the regime where the large-scale saturation prevails, the framework outlined above may still be a starting point for arranging dimensionless groups. In this regard, we have adopted, albeit provisionally, the outlook of the linear fracture mechanics (e.g. Rice, 1968; Tada *et al.*, 1985). A finite element simulation to check

the regime of validity of the small-scale saturation model is reported by Gong and Suo (1995).

4. A SOLUTION OF THE MODEL FOR AN IDEAL PARAELECTRIC

Yang and Suo (1994) took the ceramic to be a linear dielectric that distorts by the saturation strain γ_s when the electric field exceeds a certain magnitude E_s. The solution sheds insight into the phenomenon, but its accuracy remains unknown. In this section, we will analyze the small-scale saturation model on the basis of a more realistic description of paraelectrics.

An ideal paraelectric

The constitutive law for paraelectrics in Section 2 and Appendix B is complete once the nonlinear dielectric function (2.1) is prescribed. Figure 6 shows the function to be used. At a small electric field, the electric displacement increases linearly with the electric field, $D = \varepsilon E$. After the electric field exceeds a critical magnitude, E_s, the electric displacement saturates to a constant level, D_s. The three material parameters satisfy $D_s = \varepsilon E_s$. The electric displacement vector is taken to be independent of the loading history, and always parallels the electric field vector.

As mentioned before, following previous authors on the subject, we will ignore the effect of the stress on the electric displacement in (2.7). Finite element calculations of Gong (1994) show that this effect is small for a dielectric with perfect saturation. Within this simplification, the electric field is determined by this nonlinear dielectric response and the electrostatic partial differential equations in the Appendix (A.4–A.6). They specify a boundary value problem decoupled from the stress field. Once the electric displacement field is determined, it sets up a electrostrictive strain field. This strain field is in general incompatible and generates a stress field. The problem is similar to thermal stress problems. Linear superposition and many other techniques of linear elasticity theory are applicable.

The total strains are the superposition of the elastic stains and the electrostrictive

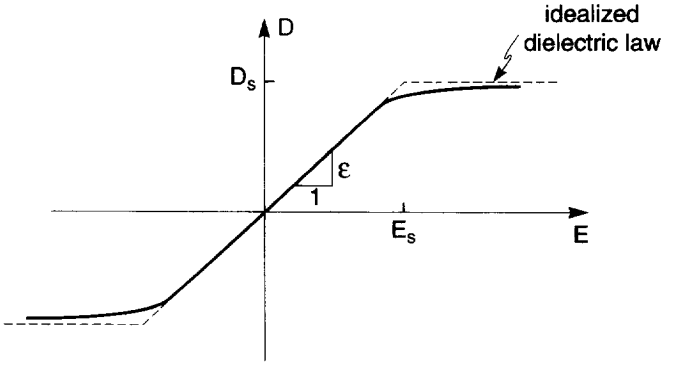

Fig. 6. A paraelectric: linearly dielectric followed by perfect polarization saturation.

strains. Appendix B gives a general formulation. Under the plane strain conditions, the strains are

$$\gamma_{11} = \frac{1-\nu^2}{Y}\left(\sigma_{11} - \frac{\nu}{1-\nu}\sigma_{22}\right) + Q[(1-q\nu)D_1^2 - q(1+\nu)D_2^2],$$

$$\gamma_{22} = \frac{1-\nu^2}{Y}\left(\sigma_{22} - \frac{\nu}{1-\nu}\sigma_{11}\right) + Q[(1-q\nu)D_2^2 - q(1+\nu)D_1^2],$$

$$\gamma_{12} = \frac{(1+\nu)}{Y}\sigma_{12} + Q(1+q)D_1D_2. \tag{4.1}$$

In the absence of stress, when the electric displacement saturates, the ceramic elongates by the strain $\gamma_s = QD_s^2$ in the direction parallel to the electric field, and contracts by the strain $q\gamma_s$ in all the directions perpendicular to the electric field.

Linear dielectrics

Yang and Suo (1994) obtained a solution around an electrode edge in a linear dielectric. Within the present material description, the solution is valid in the limit $E_s \to \infty$. This solution is the same as that derived by Smith and Warren (1966) and McMeeking (1987). The field distribution is listed explicitly as follows, and will be used later. Denote the rectangular coordinate by (x_1, x_2) and the polar coordinate by (r, θ), both centered at the electrode edge, with x_1-axis pointing directly ahead of the electrode edge. As mentioned before, the electric field is $r^{-1/2}$ singular:

$$E_1 = \frac{K_E}{\sqrt{2\pi r}}\cos\frac{\theta}{2}, \quad E_2 = \frac{K_E}{\sqrt{2\pi r}}\sin\frac{\theta}{2}, \tag{4.2}$$

where K_E is the electric intensity factor. The field lines are sketched in Fig. 5(b). The corresponding electric potential is

$$U = -K_E\sqrt{\frac{2r}{\pi}}\cos\frac{\theta}{2}. \tag{4.3}$$

This electric field induces an $1/r$ singular stress field:

$$\sigma_{11} = \frac{GC}{r}(-\beta + \cos\theta - \beta\cos 2\theta + \cos 3\theta),$$

$$\sigma_{22} = \frac{GC}{r}(-\beta + 3\cos\theta + \beta\cos 2\theta - \cos 3\theta),$$

$$\sigma_{12} = \frac{GC}{r}(-\sin\theta - \beta\sin 2\theta + \sin 3\theta), \tag{4.4}$$

where we have designated

$$G = \frac{Y}{2(1+\nu)}, \quad C = \frac{(1+q)\varepsilon^2 QK_E^2}{8\pi(1-\nu)}, \quad \beta = 2 - \frac{4q(1+\nu)}{(1+q)}. \tag{4.5}$$

The stress field is quadratic in the external load, the electric intensity K_E, as anticipated for a linear dielectric with quadratic electrostriction. The displacement field is

$$u_1 = C[(3-4\nu)\ln r + \beta\cos\theta - \tfrac{1}{2}\cos 2\theta]$$
$$u_2 = C(\beta\sin\theta - \tfrac{1}{2}\sin 2\theta) \tag{4.6}$$

The polar components of the stress field (4.4) are

$$\sigma_r = \frac{2GC}{r}(-\beta+\cos\theta), \quad \sigma_{\theta\theta} = \frac{2GC}{r}\cos\theta, \quad \sigma_{r\theta} = \frac{2GC}{r}\sin\theta. \tag{4.7}$$

The solution has a peculiar feature. Consider the semi-infinite space lying above the x_1-axis. One can readily confirm that the resultant force along the entire x_1-axis vanishes. There is, however, a finite resultant force along the semi-circle lying above the x_1-axis:

$$F_2 = \int_0^{\pi} (\sigma_r \sin\theta + \sigma_{r\theta}\cos\theta) r \, d\theta = -4\beta GC. \tag{4.8}$$

This force is pointed along the negative x_2-axis. Consequently, the semi-circle is not in equilibrium. Note that a complete circle is in equilibrium because there is a force on the lower semi-circle of the same magnitude but in the opposite direction. This feature will be removed in the following solution.

Dielectrics with perfect saturation

The above stress field is highly singular because of the two idealizations: the electrode has vanishing thickness, and the ceramic is linearly dielectric. In this section, we retain the first idealization, and modify the second with the paraelectric of perfect saturation (Fig. 6). The electric field is obtained from a well-known solution in the nonlinear fracture mechanics of a mode III crack in an elastic, perfectly-plastic material due to Hult and McClintock (1956). Hao (1994) noted that the Hult–McClintock solution is applicable for both an impermeable crack and an internal electrode. For an impermeable crack under a remote electric field perpendicular to the crack plane, the field lines are bent to parallel the crack as they approach the crack plane. Because of the exact correspondence in the governing equations and the boundary conditions, the Hult–McClintock field is valid for an impermeable crack in a paraelectric with perfect saturation, provided the anti-plane shear stresses are replaced with the electric displacements, and the strains with the electric fields. Furthermore, the semi-infinite straight line directly ahead of the impermeable crack is a constant-potential line. Consequently, the Hult–McClintock solution is also valid for a conducting sheet placed along the semi-infinite straight line. This procedure permits us to obtain solutions for nonlinear paraelectrics from elastic–plastic solutions. Rice (1968) reviewed the latter for many crack geometries. In what follows we describe in detail the field around an electrode edge in a paraelectric with perfect saturation.

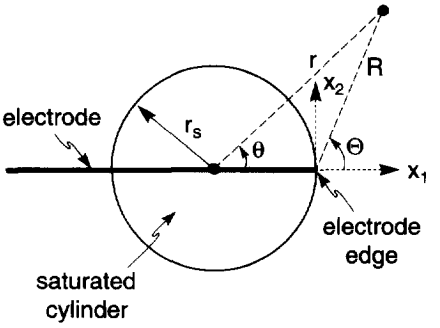

Fig. 7. The saturated cylinder centered on the electrode, its surface passing the electrode edge. Two polar coordinates are indicated, (Θ, R) centered at the electrode edge, and (θ, r) centered at the saturated cylinder center.

As shown in Fig. 7, the ceramic saturates inside a cylinder of a circular cross-section, centered on the electrode, its surface passing the electrode edge. Inside the cylinder the ceramic has the saturated electric displacement D_s; its vector direction remains to be determined. Outside the cylinder the ceramic is linearly dielectric. The electric field (4.2) is still valid outside the cylinder, but now the origin of the polar coordinate (θ, r) coincides with the center of the circle. This "new" solution clearly satisfies all the governing equations and match with the far field conditions. The ceramic on the circle has just reached the critical field, E_s. Using (4.2), we find its radius to be

$$r_s = \frac{1}{2\pi}\left(\frac{K_E}{E_s}\right)^2. \tag{4.9}$$

The electric field (4.2) is incorrect inside the cylinder. Introduce another polar coordinate (R, Θ) centered at the electrode edge (Fig. 7). We will only consider the half cylinder above the electrode because of the symmetry. On the circle, the electric field has magnitude E_s and angular distribution (4.2), so that the electric displacement is

$$D_1 = D_s \sin\Theta, \quad D_2 = -D_s \cos\Theta. \tag{4.10}$$

We have used the relation $\Theta = (\theta + \pi)/2$ for a point on the circle. Thus, on the circle, the electric displacement vector is directed in the Θ-direction and has magnitude D_s. Figure 8(a) extends (4.10) into the saturated cylinder, with the electric displacement vector perpendicular to the rays emanating from the electrode edge. This electric displacement field is clearly divergence-free. We need to find an electric potential consistent with this field.

Inside the cylinder, the electric displacement saturates, so that the electric field cannot be determined from the dielectric response in Fig. 6. Recall that the electric field relates to the gradient of the electric potential U, namely,

$$E_R = -\frac{\partial U}{\partial R}, \quad E_\Theta = -\frac{\partial U}{R\,\partial \Theta}. \tag{4.11}$$

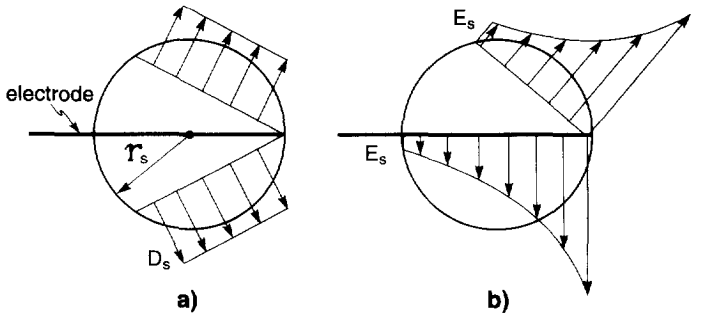

Fig. 8. The field distribution inside the saturated cylinder. Both the electric displacement and the electric field are normal to the rays emanating from the electrode edge. (a) The electric displacement has the magnitude D_s. (b) The electric field is $1/R$ singular as the edge is approached from the inside of the cylinder.

The electric field vector parallels the electric displacement vector, namely, $E_R = 0$, so that U is independent of R, but can vary with Θ. The electric potential must be continuous across the circle. From the electric potential outside the circle (4.3) and the relation $\Theta = (\theta + \pi)/2$, we find the potential on the circle:

$$U = -2r_s E_s \sin\Theta. \tag{4.12}$$

Equation (4.12) must apply inside the cylinder because U is independent of R. Its gradient gives the electric field inside the saturated cylinder:

$$\frac{E_\Theta}{E_s} = \frac{2r_s}{R}\cos\Theta, \quad E_R = 0. \tag{4.13}$$

The electric field is $1/R$ singular as a point inside the cylinder approaches the electrode edge [Fig. 8(b)]. The distributions of the electric displacement and the electric field along the x_1-axis are plotted in Fig. 9.

The stresses are derived in Appendix C and listed below. The stresses inside the saturated cylinder are

$$\sigma_{11} = \frac{GC}{r_s}\left(-\beta - 2\ln\frac{R}{r_s} + \cos 2\Theta\right),$$

$$\sigma_{22} = \frac{GC}{r_s}\left(-\beta - 2\ln\frac{R}{r_s} - \cos 2\Theta\right),$$

$$\sigma_{12} = \frac{GC}{r_s}\sin 2\Theta. \tag{4.14}$$

The total stresses outside the cylinder are

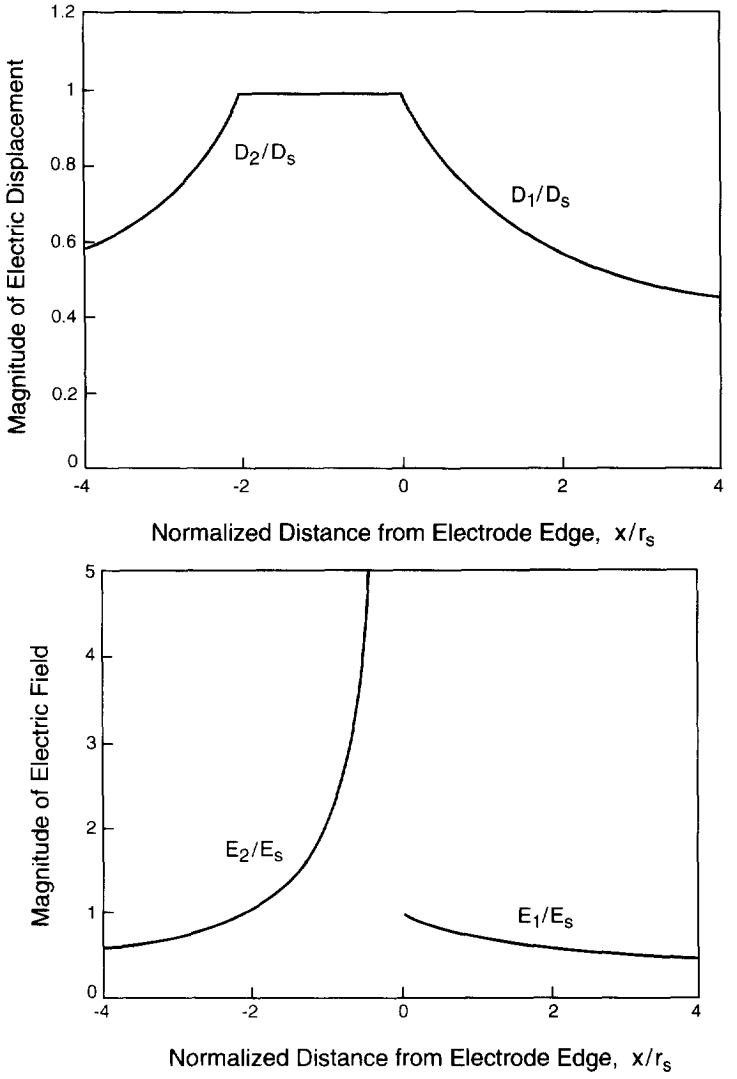

Fig. 9. (a) The magnitude of the electric displacement along the electrode and directly ahead of its edge. (b) The magnitude of the electric field.

$$\sigma_{11} = \frac{GC}{r_s}\left[2\ln\frac{r}{R} - \beta\frac{r_s}{r} - \left(\beta\frac{r_s}{r} + 1 - (1+\beta)\left(\frac{r_s}{r}\right)^2\right)\cos 2\theta + \cos 2\Theta\right],$$

$$\sigma_{22} = \frac{GC}{r_s}\left[2\ln\frac{r}{R} - \beta\frac{r_s}{r} + \left(\beta\frac{r_s}{r} + 1 - (1+\beta)\left(\frac{r_s}{r}\right)^2\right)\cos 2\theta - \cos 2\Theta\right],$$

$$\sigma_{12} = \frac{GC}{r_s}\left[-\left(\beta\frac{r_s}{r} + 1 - (1+\beta)\left(\frac{r_s}{r}\right)^2\right)\sin 2\theta + \sin 2\Theta\right]. \tag{4.15}$$

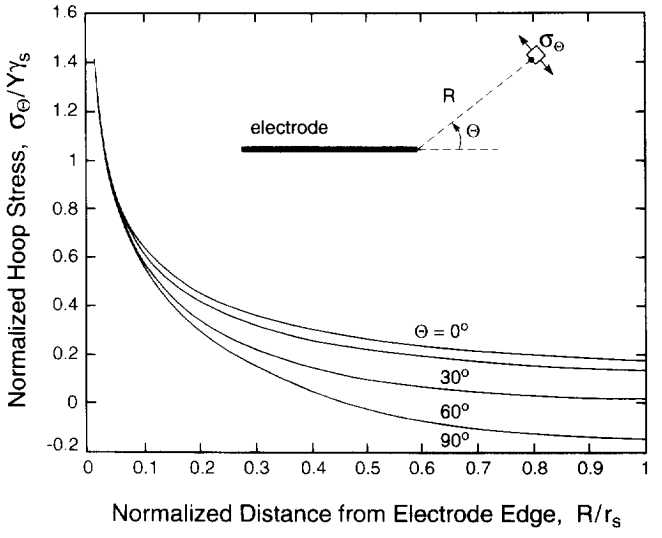

Fig. 10. The hoop stresses are logarithmic singular at the electrode edge and decay rapidly.

In the polar coordinate (R, Θ) the stresses inside the cylinder are

$$\sigma_R = \frac{GC}{r_s}\left(-\beta - 2\ln\frac{R}{r_s} + 1\right), \quad \sigma_\Theta = \frac{GC}{r_s}\left(-\beta - 2\ln\frac{R}{r_s} - 1\right), \quad \sigma_{R\Theta} = 0. \tag{4.16}$$

The stresses outside the cylinder are

$$\sigma_R = \frac{GC}{r_s}\left[2\ln\frac{r}{R} - \beta\frac{r_s}{r} + 1 - \left(\beta\frac{r_s}{r} + 1 - (1+\beta)\left(\frac{r_s}{r}\right)^2\right)\cos 2(\Theta - \theta)\right],$$

$$\sigma_\Theta = \frac{GC}{r_s}\left[2\ln\frac{r}{R} - \beta\frac{r_s}{r} - 1 + \left(\beta\frac{r_s}{r} + 1 - (1+\beta)\left(\frac{r_s}{r}\right)^2\right)\cos 2(\Theta - \theta)\right],$$

$$\sigma_{R\Theta} = \frac{GC}{r_s}\left(\beta\frac{r_s}{r} - 1 - (1+\beta)\left(\frac{r_s}{r}\right)^2\right)\sin 2(\Theta - \theta). \tag{4.17}$$

Since the origin of the polar coordinate (r, θ) now coincides with the center of the saturated cylinder, the stresses are $\ln R$ singular. The dielectric saturation makes the singularity much weaker than the $1/r$ singular field found previously for linear dielectrics. The remaining weak singularity appears to result from the idealization that the electrode has vanishing thickness. The singular term in the stress field (4.14) and (4.15) is a biaxial tension in the plane, which also induces a tensile stress σ_{33} under the plane strain conditions. See (B.8) in the Appendix. Figure 10 displays the hoop stress in (4.17). They decay rapidly away from the electrode edge. The singular term is a biaxial tension and is equal for all the orientation Θ. Because of the finite terms, for all points of the same distance R from the electrode edge, the hoop stress σ_Θ

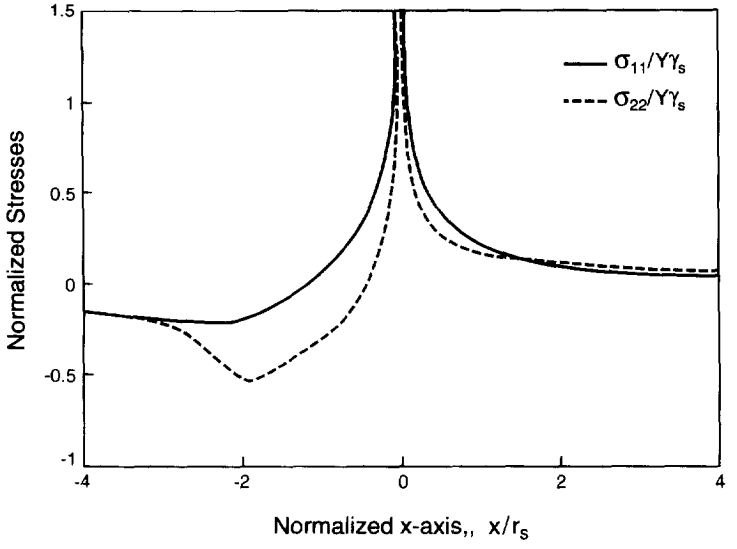

Fig. 11. The stresses in the electrode plane and in the plane directly ahead of its edge.

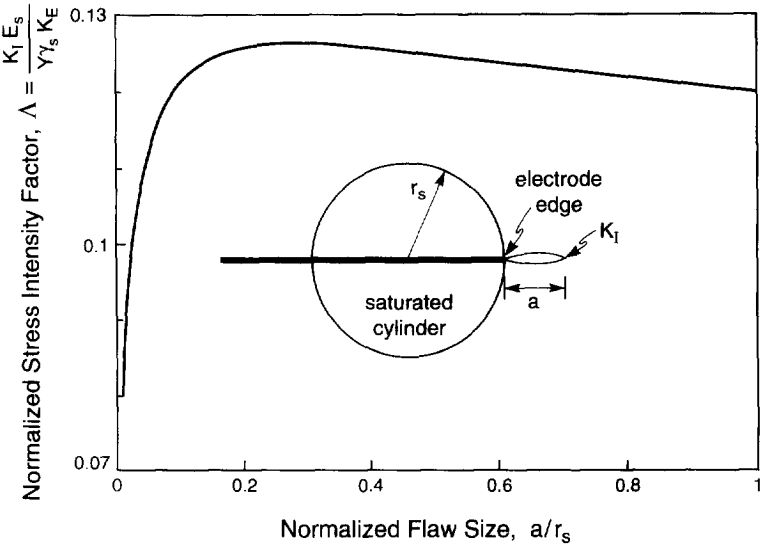

Fig. 12. The mode I stress intensity factor for flaws of various sizes near the electrode edge.

attains the maximum directly ahead of the edge. Figure 11 shows the stresses along the x_1-axis. The stress σ_{22} along the x_1-axis is not self-balanced, but gives a resultant force of magnitude $4\beta GC$. This force balances the force on the semi-circle, (4.8).

Stress intensity factor

Consider a crack-like flaw of length a directly ahead of the electrode edge (Fig. 12), where the hoop stress maximizes. The stress (4.15) induces a stress intensity factor, given by (Tada *et al.*, 1985)

$$K_{\mathrm{I}} = \sqrt{\frac{2}{\pi a}} \int_0^a \sigma_{22}(x) \sqrt{\frac{x}{a-x}}\, \mathrm{d}x. \tag{4.18}$$

Evaluating the integral (Appendix D), we obtain the stress intensity factor

$$\frac{K_{\mathrm{I}} E_{\mathrm{s}}}{Y \gamma_{\mathrm{s}} K_{\mathrm{E}}} = \frac{(1+q)\sqrt{\alpha}}{16(1-\nu^2)} \left[4\left(\ln \frac{\sqrt{\alpha+1}+1}{\sqrt{\alpha}} - \frac{1}{1+\sqrt{\alpha+1}} \right) - \frac{1+\beta}{(\alpha+1)^{3/2}} \right], \tag{4.19}$$

with $\alpha = a/r_{\mathrm{s}} = 2\pi a (E_{\mathrm{s}}/K_{\mathrm{E}})^2$. Figure 12 shows the stress intensity as a function of flaw size. The stress intensity factor vanishes for both a small and a large flaw, and peaks for a flaw of length $a = 0.28\ r_{\mathrm{s}}$. The peak value gives $\Lambda = 0.13$, where Λ is the dimensionless coefficient defined by (3.3).

If we include flaws partly on the electrode, where the stress is also tensile, we will find a larger value for Λ. In any event, our value differs somewhat from that of Yang and Suo (1994), $\Lambda = 0.19$, but the physical picture remains unchanged. It would be interesting to determine this coefficient by analyzing the small-scale saturation model for an ideal law representative of an initially unpoled ferroelectric.

5. CONCLUDING REMARKS

In this paper, we distinguish the crack nucleation from its stable growth near an internal electrode edge in a ceramic multilayer actuator. A crack nucleation model, applicable for both paraelectrics and initially unpoled ferroelectrics, is developed on the basis of the strains induced by the nonuniform electric field around the electrode edge. Only the intrinsic toughness resists a small flaw to grow; the dissipative processes such as switching or grain sliding do not contribute to the toughness. The small-scale saturation approach separates the two aspects of an actuator, the geometry and the material, making it convenient to use in design. Its regime of validity awaits a full-field nonlinear analysis. We find that, everything else being fixed, a critical layer thickness exists, below which a ceramic multilayer actuator will not crack around its internal electrode edges. A paraelectric with perfect saturation is analyzed in detail to estimate a dimensionless parameter in the model. Within the idealizations, we find that the stresses at the electrode edge are weakly singular, and are in a triaxial tensile state.

ACKNOWLEDGEMENTS

We are informed that, independent of our work, Drs C. L. Hom and N. Shankar at Martin Marietta Laboratories have recently obtained the electric field in a paraelectric with perfect saturation, and the logarithmic term of the stress field. The work of THH was supported by a visiting appointment at the University of California, Santa Barbara, funded by ONR and by the National Natural Science Foundation of China. The work of XG and ZS was supported by NSF through grant MSS-9258115, and by ONR through contract N00014-93-1-0110.

REFERENCES

Aburatani, H., Harada, S., Uchino, K. and Furuta, A. (1994) Destruction mechanism of ceramic multilayer actuators. *Japanese J. Appl. Phys.* **33,** 3091–3094.

Cao, H. C. and Evans, A. G. (1993) Nonlinear deformation of ferroelectric ceramics. *J. Am. Ceram. Soc.* **76,** 890–896.

Cao, H. C. and Evans, A. G. (1994) Electric-field-induced fatigue crack growth in piezoelectrics. *J. Am. Ceram. Soc.* **77,** 1783–1786.

Furuta, A. and Uchino, K. (1993) Dynamic observation of crack propagation in piezoelectric multilayer actuators. *J. Am. Ceram. Soc.* **76,** 1615–1617.

Gong, X. (1994) Stresses near the end of an internal electrode in multilayer electrostrictive ceramic actuators. *Mater. Res. Soc. Symp. Proc.* **360.**

Gong, X. and Suo, Z. (1995) Finite element simulation for the reliability of nonlinear ceramic multilayer actuators. (submitted.)

Haertling, G. H. (1987) PLZT electrooptic materials and applications—a review. *Ferroelectrics* **75,** 25–55.

Hao, T. H. (1994) Unpublished work.

Hom, C. L. and Shankar, N. (1994) A fully coupled constitutive model for electrostrictive ceramic materials. *J. Intelligent Mater. Systems Struct.* **5,** 795–801.

Hult, J. A. M. and McClintock, F. A. (1956) Elastic–plastic stress and strain distribution around sharp notches under repeated shear. *Proc. Ninth Int. Congr. Applied Mechanics* **8,** Belgium, pp. 51–58.

Jaffe, B., Cook, W. R. and Jaffe, H. (1971) *Piezoelectric Ceramics*. Academic Press, New York.

Jang, S. J., Uchino, K., Nomura, S. and Cross, L. E. (1980) Electrostrictive behavior of lead magnesium niobate based ceramic dielectrics. *Ferroelectrics* **27,** 31–34.

Jona, F. and Shirane, G. (1962) *Ferroelectric Crystals*. Pergamon Press, Oxford.

Lange, F. F. (1974) Criteria for crack extension and arrest in residual localized stress fields associated with second phase inclusions. *Fracture Mechanics of Ceramics*, Vol. 2, pp. 599. Plenum Press.

Lu, T. C., Yang, J., Suo, Z., Evans, A. G., Hecht, R. and Mehrabian, R. (1991) Matrix cracking in intermetallic composites caused by thermal expansion mismatch. *Acta Metall. Mater.* **39,** 1883–1890.

Lynch, C. S. (1995) The effect of uniaxial stress on the electro-mechanical response of 8/65/35 PLZT. Submitted to *Acta Metall. Mater.*

Lynch, C. S., Yang, W., Collier, L., Suo, Z., and McMeeking, R. M. (1995) Electric field induced cracking in ferroelectric ceramics. *Ferroelectrics* **166,** 11–30.

McMeeking, R. M. (1987) On mechanical stresses at cracks in dielectrics with application to dielectric breakdown. *J. Appl. Mech.* **62,** 3116–3122.

Muskhelishvili, N. I. (1963) *Some Basic Problems of the Mathematical Theory of Elasticity*. Noordhoff, Netherlands.

Pan, W. Y., Dam, C. Q., Zhang, Q. M. and Cross, L. E. (1989) Large displacement transducers based on electric field forced phase transition in the tetragonal $(Pb_{0.97}La_{0.02})$ (Ti, Zr, Sn)O_3 family of ceramics. *J. Appl. Phys.* **66,** 6014–6023.

Rice, J. R. (1968) Mathematical analysis in the mechanics of fracture. *Fracture*, Vol. II (ed. H. Liebowitz). Academic Press, New York.

Schneider, G. A., Rostek, A., Zickgraf, B. and Aldinger, F. (1994) Crack growth in ferroelectric ceramics under mechanical and electrical loading. *Proc. 4th, Int. Congr. Electronic Ceramics & Appl.*, pp. 1211–1216.

Smith, T. E. and Warren, W. E. (1966) Some problems in two-dimensional electrostriction. *J. Math. Phys.* **45,** 45–51; **47,** 109–110 (1968) (corrigenda).

Sundar, V. and Newnham, R. E. (1992) Electrostriction and polarization. *Ferroelectrics* **135,** 431–446.

Suo, Z. (1991) Mechanics concepts for failure in ferroelectric ceramics. *Smart Structures and Materials* (ed. A. V. Srinvasan), pp. 1–6. ASME, New York.

Suo, Z. (1993) Models for breakdown resistant dielectric and ferroelectric ceramics. *J. Mech. Phys. Solids* **41,** 1155–1176.

Tada, H., Paris, P. C. and Irwin, G. R. (1985) *The Stress Analysis of Cracks Handbook*. Del Research, St. Louis, MO

Uchino, K. (1993) Ceramic actuators: principles and applications. *MRS Bulletin*, April Issue, 42–48.

White, G. S. and Friedman, S. W. (1994) Intelligent ceramic materials: issues of brittle fracture. *Proc. 2nd Int. Conf. Intelligent Materials*, pp. 52–62. Technomics Publisher, Williamsburg, Virginia.

Winzer, S. R., Shankar, N. and Ritter, A. P. (1989) Designing cofired multilayer electrostrictive actuators for reliability. *J. Am. Ceram. Soc.* **72**, 2246–2257.

Yang, W. and Suo, Z. (1994) Cracking in ceramic actuators caused by electrostriction. *J. Mech. Phys. Solids* **42** 649–663.

Yoshikawa, S. and Shrout, T. (1993) Multilayer piezoelectric actuators—structures and reliability. American Institute of Aeronautics and Astronauts (AIAA)-93-1711-CP.

APPENDIX A: PARTIAL DIFFERENTIAL EQUATIONS FOR STATIC FIELDS

Let u_i be the displacement vector and γ_{ij} the strain tensor. Geometric compatibility requires that

$$\gamma_{ij} = \tfrac{1}{2}(u_{i,j} + u_{j,i}). \tag{A.1}$$

The usual index notation is adopted. When the external body forces are negligible, mechanical equilibrium requires that the stress tensor σ_{ij} be divergence-free inside a material,

$$\sigma_{ij,j} = 0, \tag{A.2}$$

and jumps across an interface between two materials by

$$n_i[\sigma_{ij}^{+} - \sigma_{ij}^{-}] = t_i, \tag{A.3}$$

where n_i is the unit normal vector of the interface pointing from material + to material −, and t_i the external traction on the interface.

The static electric field E_i is the gradient of the electric potential U:

$$E_i = -U_{,i}. \tag{A.4}$$

When the external body charge is negligible, the electric displacement vector D_i is divergence-free in a dielectric,

$$D_{i,i} = 0, \tag{A.5}$$

and jumps across an interface between two materials by

$$n_i[D_i^{+} - D_i^{-}] = -\omega, \tag{A.6}$$

where ω is the external charge on unit area of the interface.

APPENDIX B: CONSTITUTIVE LAW FOR ISOTROPIC PARAELECTRICS

Let $\psi(\mathbf{D}, \gamma)$ be the Helmholtz free energy per unit volume at a fixed temperature and

$$d\psi = E_i dD_i + \sigma_{ij} d\gamma_{ij}. \tag{B.1}$$

The electric field vector **E** and the stress tensor σ are the differential coefficients of the free energy. Define the elastic Gibbs free energy per unit volume by

$$g = \psi - \sigma_{ji}\gamma_{ij} \tag{B.2}$$

For a small increment in the electric displacement and the stress, g varies by

$$dg = E_i dD_i - \gamma_{ij} d\sigma_{ji}. \tag{B.3}$$

The elastic Gibbs energy is a function of the electric displacements and stresses, $g(\mathbf{D}, \sigma)$, and the electric fields and strains are its differential coefficients:

$$E_i = \frac{\partial g}{\partial D_i}, \quad \gamma_{ij} = -\frac{\partial g}{\partial \sigma_{ji}}. \tag{B.4}$$

Suo (1991) introduced the following function for an isotropic paraelectric:

$$g(\mathbf{D}, \sigma) = -\frac{1}{Y}[(1+\nu)\sigma_{ji}\sigma_{ji} - \nu\sigma_{mm}\sigma_{nn}] - Q[(1+q)\sigma_{ji}D_iD_j - q\sigma_{mm}D_nD_n] + \int_0^D f(\Delta)d\Delta \tag{B.5}$$

Here $D = (D_nD_n)^{1/2}$ is the magnitude of the electric displacement. Taking the differentiation in (B.4) we obtain

$$\gamma_{ij} = [(1+\nu)\sigma_{ij} - \nu\sigma_{mm}\delta_{ij}]/Y + [(1+q)D_iD_j - qD_nD_n\delta_{ij}]Q. \tag{B.6}$$

and

$$E_i = -2[(1+q)\sigma_{ij}D_j - q\sigma_{mm}D_i]Q + D_i f(D)/D \tag{B.7}$$

where Kronecker's delta $\delta_{ij} = 0$ when $i \neq j$, and $\delta_{ij} = 1$ when $i = j$. They reproduce the behaviors under the uniaxial loads described in Section 2.

Under the plane strain conditions, the electric field, the electric displacements, and the displacements lie in the (x_1, x_2)-plane. From $\gamma_{33} = 0$, we find that

$$\sigma_{33} = \nu(\sigma_{11} + \sigma_{22}) + YQq(D_1^2 + D_2^2). \tag{B.8}$$

Substituting (B.8) into (B.6) gives (4.1).

APPENDIX C: ADD STRESSES TO MATCH THE CYLINDER WITH ITS SURROUNDING

In Section 4, we divide the ceramic into a saturated cylinder and the material outside. The stresses (4.4) and the displacements (4.6) constitute an equilibrium, compatible field outside the cylinder. The electric displacements (4.10) give rise to a stress-free deformation field inside the cylinder. The two fields do not match along the circle. To match the displacements and resultant forces, we add stress fields to the ceramic both inside and outside the cylinder.

We use the complex variable methods (Muskhelishivili, 1963) to determine these additional stress fields. The equilibrium, compatible, plane-strain field in an isotropic, linearly elastic solid can be represented by two analytic functions $\phi(z)$ and $\psi(z)$, with $z = re^{i\theta}$ and $i = \sqrt{-1}$. The stresses, the displacements, and the resultant forces on an arc are calculated from the two functions according to

$$\frac{\sigma_{22} + \sigma_{11}}{2} = \phi'(z) + \bar{\phi}'(\bar{z}), \tag{C.1}$$

$$\frac{\sigma_{22}-\sigma_{11}}{2}+i\sigma_{12}=\bar{z}\phi''(z)+\psi'(z), \tag{C.2}$$

$$2G(u_1+iu_2)=(3-4\nu)\phi(z)-z\bar{\phi}'(\bar{z})-\bar{\psi}(\bar{z}), \tag{C.3}$$

$$F_1+iF_2=-i[\phi(z)+z\bar{\phi}'(\bar{z})+\bar{\psi}(\bar{z})]. \tag{C.4}$$

Denote the points along the circle by $t=r_s e^{i\theta}$. The displacements (4.6) on the circle are

$$u_1+iu_2=C[\beta(e^{i\theta}-1)-\tfrac{1}{2}(e^{2i\theta}-1)]. \tag{C.5}$$

Rigid body displacements are added so that the material at the electrode edge does not translate and the electrode does not rotate. The resultant force due to stresses (4.4) along the circle is

$$F_1+iF_2=-iGC[-2\beta(e^{i\theta}-1)+(e^{2i\theta}-1)]. \tag{C.6}$$

The electric displacement inside the cylinder, Fig. 8(a), induces a strain field. Under the plane strain conditions, the electrostrictive strains inside the cylinder are

$$\gamma_\Theta=(1-q\nu)\gamma_s, \quad \gamma_R=-(1+\nu)q\gamma_s, \quad \gamma_{R\Theta}=0. \tag{C.7}$$

These strains give rise to a stress-free, compatible deformation

$$u_R=-(1+\nu)q\gamma_s R, \quad u_\Theta=(1+q)\gamma_s R(\Theta-\pi). \tag{C.8}$$

The rigid-body displacement is chosen such that the electrode edge does not displace and the whole electrode does not rotate. In the rectangular components, the above displacements on the circle are

$$u_1+iu_2=e^{i\Theta}(u_R+iu_\Theta)=\tfrac{1}{2}(1+q)\gamma_s r_s(e^{i\theta}-1)\left(\frac{\beta}{2}-1-i\pi+i\theta\right). \tag{C.9}$$

We have used the relation $\Theta=(\theta+\pi)/2$ for a point on the circle.

The above displacements and forces mismatch on the circle. We next add field $\phi_1(z)$ and $\psi_1(z)$ inside the cylinder, and add field $\phi_2(z)$ and $\psi_2(z)$ outside the cylinder. The functions must satisfy the following conditions: (I) The total displacements and resultant forces must be continuous across the circle. (II) Except at the electrode edge $z=r_s$, $\phi_1(z)$ and $\psi_1(z)$ are analytic inside the circle, and $\phi_2(z)$ and $\psi_2(z)$ are analytic outside the circle. (III) The added stress field causes vanishing displacements or rotation at the infinity, so that $\phi_2(z)$ and $\psi_2(z)$ vanish at the infinity.

Continuity of displacements and the resultant forces require that

$$(3-4\nu)\phi_1(t)-t\bar{\phi}_1'(\bar{t})-\bar{\psi}_1(\bar{t})+G(1+q)\gamma_s r_s(e^{i\theta}-1)\left(\frac{\beta}{2}-1-i\pi+i\theta\right)$$

$$=(3-4\nu)\phi_2(t)-t\bar{\phi}_2'(\bar{t})-\bar{\psi}_2(\bar{t})+GC[2\beta(e^{i\theta}-1)-(e^{2i\theta}-1)] \tag{C.10}$$

and

$$\phi_1(t)+t\bar{\phi}_1'(\bar{t})+\bar{\psi}_1(\bar{t})=\phi_2(t)+t\bar{\phi}_2'(\bar{t})+\bar{\psi}_2(\bar{t})+GC[-2\beta(e^{i\theta}-1)+(e^{2i\theta}-1)]. \tag{C.11}$$

The sum of (C.10) and (C.11) gives the jump condition

$$\phi_2(t)-\phi_1(t)=GC(e^{i\theta}-1)\left(\frac{\beta}{2}-1-i\pi+i\theta\right). \tag{C.12}$$

Substitution of (C.12) into (C.11) gives the jump condition

$$\psi_2(t)-\psi_1(t)=GC\left[(1+\beta)e^{i\theta}-\frac{3\beta}{2}+i\pi-i\theta\right]. \tag{C.13}$$

Equations (C.12) and (C.13) ensure that both the displacement and the resultant force will be continuous across the circle (Condition I). Condition II is satisfied as follows.

Note that, for a point on the circle, $t = r_s e^{i\theta}$ and

$$i\theta = \ln \frac{t}{r_s} = \ln \frac{t}{t-r_s} + \ln \frac{t-r_s}{r_s}.$$

On the right-hand side, the first function analytically extends into the region $|z| > r_s$ if a branch-cut is drawn from point $z = 0$ to point $z = r_s$. The second function analytically extends into region $|z| < r_s$ if a branch cut is drawn from point $z = r_s$ to the infinity. One can readily confirm that the two functions

$$\phi_1(z) = -GC\left(\frac{z}{r_s} - 1\right)\left(\frac{\beta}{2} - 1 - i\pi + \ln \frac{z-r_s}{r_s}\right) - GC, \tag{C.14}$$

$$\phi_2(z) = GC\left(\frac{z}{r_s} - 1\right)\ln \frac{z}{z-r_s} - GC, \tag{C.15}$$

satisfy the jump condition (C.12) and Condition II. The constants are added to satisfy Condition III. Using the similar procedure to the jump condition (C.13) we find that

$$\psi_1(z) = GC\left(\frac{\beta}{2} - i\pi + \ln \frac{z-r_s}{r_s}\right). \tag{C.16}$$

$$\psi_2(z) = GC\left[(1+\beta)\frac{r_s}{z} - \ln \frac{z}{z-r_s}\right]. \tag{C.17}$$

These functions give the stresses (4.14) inside the circle and, in addition to (4.4), the total stresses (4.15) outside the circle.

APPENDIX D: TWO INTEGRALS

In evaluating the stress intensity factor (4.19), we encountered two definite integrals, which we evaluated by contour integrals on the complex plane. The answers are

$$\int_0^\alpha \left(\frac{x}{\alpha - x}\right)^{1/2} \ln\left(\frac{x+1}{x}\right) dx = \pi\alpha\left(\ln \frac{\sqrt{\alpha+1}+1}{\sqrt{\alpha}} - \frac{1}{1+\sqrt{\alpha+1}}\right), \tag{D.1}$$

$$\int_0^\alpha \left(\frac{x}{\alpha - x}\right)^{1/2} \frac{dx}{(x+1)^2} = \frac{\pi\alpha}{2(\alpha+1)^{3/2}}. \tag{D.2}$$